High-pressure x-ray and Raman studies of rubidium and cesium graphite intercalation compounds

N. Wada*
The Department of Physics and James Franck Institute, University of Chicago, Chicago, Illinois 60637
(Received 24 November 1980)

Systematic pressure-dependence studies have been performed on MC_8 and MC_{12n} (M = Rb, Cs and n = 2, 3, 4) graphite intercalation compounds. Pressure-induced staging phase transitions similar to that which had been previously reported for KC_{24} by Clarke *et al.* were found in these high-stage graphite intercalation compounds ($n \geq 2$). The $\vec{q} \perp c$ x-ray experiments revealed the formation of a 2×2 superlattice under hydrostatic pressure from the disordered intercalant layers at ambient conditions. The Raman spectra from RbC_{12n} (n = 2, 3, 4) gave clear evidence for the pressure-induced staging transition by showing a change in the Raman intensities of the bounding (1605 cm^{-1}) and interior (1582 cm^{-1}) E_{2g}-like phonon peaks with pressure. In addition, the compressibilities k_d of CsC_8 and RbC_8 were measured as (1.56 ± 0.05) and $(2.42 \pm 0.12) \times 10^{-12}$ cm^2/dyn, respectively. The compressibility results indicate that the interlayer-coupling strength varies drastically among alkali-graphite intercalation compounds. The pressure-dependent Raman spectra of RbC_8 showed an appreciable change in the Fano resonance shape at ~ 580 cm^{-1} with pressure. The mode-Grüneisen constant $\gamma_{0\perp}$ of pristine graphite for the for the interlayer mode E_{2g} was found to be 1.66 ± 0.13. The rates of Raman frequency shifts with respect to pressure, $\partial\omega_0/\partial P$, were measured to be (0.70 ± 0.12), (0.51 ± 0.09), (0.44 ± 0.05), (0.54 ± 0.08) cm^{-1} $kbar^{-1}$ for the bounding modes of CsC_{24} and RbC_{12n} (n = 2, 3, 4), and (0.78 ± 0.08), (0.32 ± 0.12) cm^{-1} $kbar^{-1}$ for the interior modes of RbC_{12n} (n = 3, 4), respectively.

I. INTRODUCTION

Graphite intercalation compounds (GIC's) have recently stimulated much interest as synthetic metals with two-dimensional (2D) characteristics.[1] Because of their highly anisotropic structures, variety of intercalant species, and staging mechanism, these lamellar compounds afford a rich opportunity for studying structural phase transitions, especially those related to low dimensionality and dimensionality-crossover phenomena.[2-6]

Alkali-metal graphite intercalation compounds (AGIC's) are the best-investigated materials among the donor compounds, because AGIC's have relatively simple structures and can be obtained as a "pure stage"-n compound.[7] (A stage-n compound consists of an alternating sequence of n hexagonal graphite layers and an intercalant layer. When a compound has one phase of this long-range sequence, it is called "pure.") Stage-1 AGIC's have an ideal bulk stoichiometry of MC_8 (M = K, Rb, and Cs), in which alkali-metal intercalant atoms form a 2×2 triangular superlattice on the matrix of graphite layers. Stage-1 AGIC's are well defined 3D crystals at room temperature.[8] Note, however, that recent theory[9] and experiment[10] have showed that the stoichiometry of stage-1 AGIC's can be continuously varied with temperature and alkali-metal vapor pressure. Stage-2 or higher-stage compounds have an ideal bulk stoichiometry of MC_{12n} (M = K, Rb, and Cs and $n = 2, 3, 4, \ldots$, where n designates the stage of a compound). The intercalant layers are disordered at ambient conditions, and researchers have found evidence for both a quasi-2D liquid-like[2,4,11] and a lattice-gas-type[3,5,12] disorder. The nature of short-range ordering and its relationship to stoichiometry and staging are interesting and controversial subjects in high-stage AGIC's ($n \geq 2$).

Recently, Safran and Hamann[13] proposed an elastic dipole theory for staging, in which elastic dipoles created by intercalant atoms between the hexagonal graphite layers are responsible for the attractive intralayer interaction and repulsive interlayer interaction. The elastic theory naturally suggests that external pressure should increase the strength of elastic dipoles and, hence, of intra- and interlayer interactions. Therefore, one might anticipate structural phase transitions to occur in GIC's under high pressure.

In fact, Clarke, Wada, and Solin[14] observed a pressure-induced staging phase transition in stage-2 KC_{24}. Under hydrostatic pressure, stage-2 KC_{24} transformed to pure stage-3 KC_{24}. The coexistence of two phases was observed over a wide pressure range. It was concluded that the disordered potassium layers at ambient conditions (layer stoichiometry of KC_{12}) became ordered to form a 2×2 in-plane superlattice (layer stoichiometry of KC_8) under high pressure (3–6 kbar). Simultaneously, the stacking sequence changed from that characteristic of stage 2 to that of stage 3 with the bulk stoichiometry of KC_{24} fixed. (Note

that a stage-3 compound with a layer stoichiometry KC_8 also yields a bulk stoichiometry of KC_{24}; $KC_{2\times12} = KC_{3\times8}$). The transition was found to be completely reversible, hysteretic, and of first order. The sample dependence of the staging transition was attributed to defects in the samples.

The Raman scattering technique has been extensively used to extract information on phonon dynamics as well as charge delocalization in GIC's.[15-20] Although the hexagonal graphite layer structure experiences changes such as a layer distortion[12] and an expansion of the carbon-carbon (C–C) distance[21] upon intercalation, the strong coplanar covalent bonds of C atoms persist. As a result, the well pronounced intraplanar Raman-active mode E_{2g} of pristine graphite (1582 cm^{-1}) shows only slight frequency shifts upon intercalation. Nemanich, Solin, and Guérard[16] postulate a "nearest-layer" model (NL model) which was successfully applied to interpret the stage dependence of the Raman spectra of donor and acceptor GIC's. They classified the graphite layers into three types: type A, graphite layer bounded by a pair of intercalant layers, type B, bounded by an intercalant layer and another graphite layer, and type C, bounded by other graphite layers as in the case of pristine graphite. Stage-1 compounds contain only type-A graphite layers, whereas stage-2 compounds contain only type-B graphite layers. Stage-n compounds ($n \geq 3$) contain a mixture of type-B and -C layers.

Correspondingly, stage-2 compounds exhibit one E_{2g}-like Raman peak at ~1605 cm^{-1}, whereas stage-n compounds ($n \geq 3$) exhibit two E_{2g}-like peaks; one at ~1610 cm^{-1} originating from type-B layers (bounding mode), and the other at ~1583 cm^{-1} from type-C layers (interior mode). The relative ratio of the integrated Raman intensity of the bounding mode to the interior mode was shown to be proportional to the ratio of the number of type-B layers to type-C layers.[16] Therefore, we should be able to observe an evolution of the interior peak in stage-2 compounds, and a change in the ratio of the interior mode and bounding mode Raman intensities in higher-stage compounds ($n \geq 3$), if we induce staging phase transitions to higher stage in GIC's.

Stage-1 AGIC's exhibit quite different Raman spectra from high-stage AGIC's ($n \geq 2$). They contain two Fano resonances in the spectra.[15-20] The features at ~1500 cm^{-1} have been attributed to the Fano resonance of a graphite E_{2g}-like mode with a continuum.[17] In a recent theory by Miyazaki *et al.*,[22] the interaction of symmetry-allowed phonons at 858, 1280, and 1580 cm^{-1}, with the electronic interband excitation between the split graphite π bands in stage-1 compounds, accounts for the Fano resonance at ~1500 cm^{-1}. The Fano resonance of CsC_8 at ~580 cm^{-1} was carefully examined by Caswell and Solin,[18] who found that it was disorder induced and originated from single phonon excitation.

In this paper, we report x-ray and Raman work on Rb and Cs intercalated graphite systems under hydrostatic pressure up to 10 kbar. We will focus on pressure-induced in-plane ordering of intercalant atoms and staging phase transitions, especially in higher-stage compounds ($n \geq 3$). Quantitative properties of these compounds, such as compressibilities and pressure-induced Raman frequency shifts, will also be discussed. Experimental apparatus and procedures are described in Sec. II. Sections III and IV deal with x-ray and Raman results and discussion, respectively. Concluding remarks are given in Sec. V.

II. EXPERIMENTAL

A. Sample preparation

All the samples used in this experiment were prepared from single-crystal graphite, using the Hérold two-bulb method.[23] Each single crystal was cut with a razor blade and had an approximate size of $0.35 \times 0.35 \times 0.05$ mm^3. Details of our intercalation procedure have been described elsewhere.[15] Note here that single-crystal samples are superior to the highly oriented pyrolytic graphite (HOPG) for exploring the in-plane structures of GIC's. Since HOPG consists of microcrystals of dimension ~1 μm with their crystalline c axes oriented in one direction (to within less than 1°) and their a axes oriented randomly in the basal plane, it gives rise to powder averaged in-plane diffracted x-ray rings.

Bassett diamond-anvil cells[24] with a Be-Cu gasket were employed to generate hydrostatic pressure up to 10 kbar for both Raman and x-ray measurements. A schematic diagram of the cell with a typical x-ray scattering geometry is shown in Fig. 1. For Raman scattering, instead of Be supporting bases, hard-steel bases with tapered holes for scattered light collection were used. This cell was also used for some of the $\vec{q} \perp c$ x-ray scattering, though the scan angles were not as wide as the cell with Be bases. Hydrostatic pressure was calibrated before and after each measurement by the ruby fluorescence technique.[25] The estimated error was ±0.5 kbar.

Special precautions have to be taken when handling AGIC's, since they are known to be more chemically active than virgin alkali metals. Especially for Raman scattering, the good surface condition is crucial, since the penetration depth of visible light is $\lesssim$1000 Å.[15] Heavy mineral oil which had been vacuum-degassed was found to be

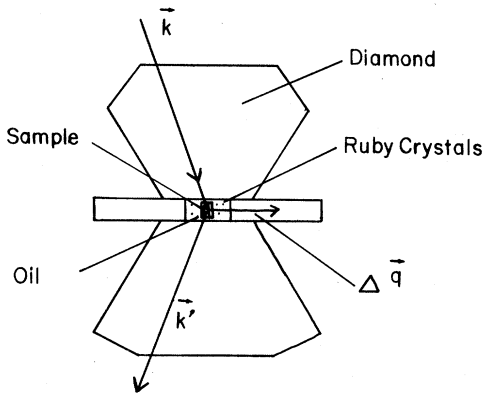

FIG. 1. Schematic representation of the gasketed diamond anvil apparatus.

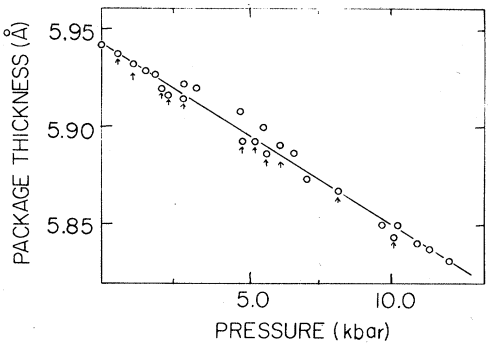

FIG. 2. Package thickness of CsC_8 as a function of hydrostatic pressure. The circles without an arrow show the first-run data points, which were taken consecutively up to the highest pressure. The arrows indicate the second-run data points from the same sample. The straight line was obtained from the least-squares analysis of the data points.

nonreactive with AGIC's and so was used as a pressure-transmitting medium. The stage of each sample was determined by x-ray diffraction. It was then sealed in a Pyrex tube. In an Ar-gas-filled glove bag, the tube was broken under the surface of the cleaned oil, and the sample was transferred to the gasket chamber. After adding several ruby crystals (~10 μm in size) to the chamber, the cell was closed with minimal pressure. The whole sample transfer procedure took less than 30 minutes. With a successful operation no color change or bubbling of the sample was observed. No sample degradation was detected by either x-ray or Raman scattering in the diamond anvil cell, even after several weeks.

X-ray diffraction measurements were carried out on a Picker four-circle automatic diffractometer with a Rigaku 12-kW rotating anode x-ray generator, using Mo $K\alpha$ x rays ($\bar{\lambda}=0.71069$ Å). Raman spectra were taken in the true backscattering configuration, using a point-focused 5145-Å Ar-ion laser incident beam and a Jarrel Ash Model 25-100 double monochromator equipped with Jobin Yvon holographic gratings. Since AGIC's can be damaged by strong laser power,[15] it was limited to ~15 mW. To minimize the fluorescent background from the diamonds and mineral oil, the polarization of incident and scattered light were always kept in the crossed configuration.[26] Details of the high-pressure Raman technique can be found elsewhere.[25]

III. X-RAY RESULTS AND DISCUSSION

A. Stage 1

The package thickness d, or the distance along the c axis between the two nearest intercalant layers, can be determined by measuring the (00l) Bragg peak positions. Figure 2 shows the data of package thickness of stage-1 CsC_8 as a function of pressure at room temperature. From the slope of the least-squares best fit straight line, the compressibility k_d (Ref. 27) of CsC_8 can be obtained. Here, the compressibility k_d is defined as

$$k_d \equiv \frac{1}{d_0}\left(\frac{\partial d}{\partial P}\right)_{P=0}, \tag{1}$$

where d is a package thickness and P is the pressure. (Note that the coplanar covalent bonds of carbon atoms are so strong that we may neglect the in-plane contraction at pressures less than 10 kbar.) The compressibility k_d for CsC_8 was found to be $(1.56\pm0.05)\times10^{-12}$ cm^2/dyn. "First-run" data points in Fig. 2, where the sample did not experience the highest pressure, show some deviation from the straight line at a pressure range of 3–6 kbar. The "second-run" data (taken after reaching the highest pressure) seem to obey Hooke's law. This deviation of first-run data might be related to an unstable stacking sequence[10] found in CsC_8. Thus it appears that the sample experienced pressure annealing.

The x-ray compressibility results for stage-1 RbC_8 are shown as a plot of package thickness versus pressure in Fig. 3. Above ~7.5 kbar, an apparent deviation from Hooke's law can be seen in the figure, indicating a saturation effect. From the slope of the straight line, the compressibility of RbC_8 was found to be $(2.42\pm0.12)\times10^{-12}$ cm^2/dyn.

For comparison, the compressibilities of pristine graphite[27] and MC_8 [M=K (Ref. 27), Rb, and Cs] are tabulated in Table I. It is surprising that there is a wide variation among the compres-

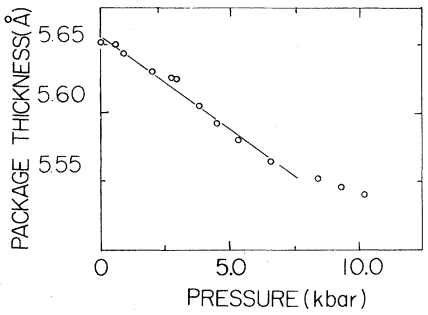

FIG. 3. Package thickness of RbC_8 as a function of hydrostatic pressure. The straight line indicates the least-squares best fit of the data points below 7 kbar.

sibilities of stage-1 AGIC's. CsC_8 was found to be the "hardest." It showed about a 75% increase in the c-axis force constant relative to graphite. By contrast, RbC_8 showed just a 13% increase. (Note that Ellenson *et al.*[28] obtained a 20% increase in the RbC_8 c-axis force constant relative to graphite by neutron scattering. We believe that our method gives more accurate compressibility values than the technique employed by Elleson *et al.*[28]) This wide variation among the compressibilities indicates that the strengths of interlayer coupling, or the overlaps of intercalant s electrons and graphite π electrons, differ substantially among stage-1 AGIC's.

The observed differences are consistent with the resistivity measurements by Fuerst *et al.*[29] They found that the c-axis resistivity of KC_8 (3.3×10^{-4} Ω cm) was larger than that of CsC_8 (2×10^{-4} Ω cm) at room temperature, whereas their a-axis resistivities are similar. This implies that the interlayer coupling in CsC_8 is stronger than in KC_8. (No data for the RbC_8 c-axis resistivity is available.)

In the compressibility experiments on CsC_8 and RbC_8, we did not find any evidence for a phase transition. The $\vec{q}\perp c$ x-ray experiments on CsC_8 also revealed the 2×2 in-plane superlattice, but

TABLE I. The compressibility (k_d), the zero pressure package thickness (d_0), and the coefficient of least-squares determination (R^2).

	k_d (10^{-12} cm^2/dyn)	d_0 (Å)	R^2
Graphite[a]	2.73 ± 0.09	3.353 ± 0.003	0.990
KC_8[a]	2.13 ± 0.09	5.355 ± 0.004	0.986
RbC_8[b]	2.42 ± 0.12	5.657 ± 0.007	0.981
CsC_8	1.56 ± 0.05	5.943 ± 0.004	0.979

[a] Reference 27.
[b] The data points below 7 kbar were used.

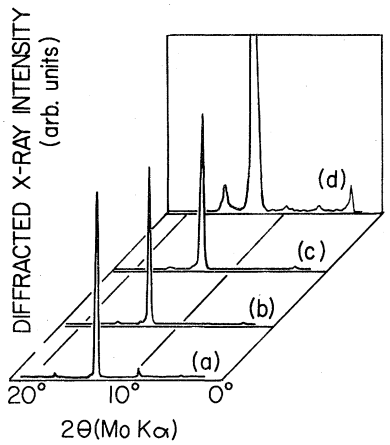

FIG. 4. (00l) x-ray profiles of CsC_{24} taken at (a) 1.1, (b) 5.7, and (c) 8.5 kbar. The profile (d) shows the expansion of (c). The small peak next to the pronounced peak at $2\theta\simeq13°$ was due to stage-1 regions on the surface of the sample.

no other superlattice structures were observed up to at least 10 kbar. Note, in particular, that no evidence was found for a $\sqrt{3}\times\sqrt{3}$ superlattice.[30] The a-axis compressibility was negligible.

B. Stage 2

Figure 4 shows the (00l) x-ray profiles of CsC_{24} taken at different pressures. The x-ray profile (a) at 1.1 kbar can be indexed as that of stage-2 CsC_{24}. (The small peak next to the $2\theta\simeq13°$ Bragg peak of CsC_{24} was due to stage-1 regions on the surface of the sample. It was difficult to make pure stage-2 CsC_{24}, since the sample's surface tended to intercalate to stage 1 while the sample cooled in the intercalation process. Note that our sample was quite small.) Although these (00l) profiles do not show the staging transition as dramatically as those in KC_{24},[14] new stage-3 Bragg peaks can be observed at ~5 kbar growing at the expense of the stage-2 peaks. The expansion of the x-ray profile at 8.5 kbar indicates that the sample has transformed to stage 3. In order to see the staging phase transition more clearly, the package thickness versus pressure was plotted in Fig. 5. Here, the pronounced Bragg peak at $2\theta\simeq13°$ was used to calculate the package thickness d with Bragg's law. The appearance of stage-3 domains is now perceived as an increase in the package thickness at ~5 kbar in Fig. 5. (Note that stage-3 CsC_{24} gives rise to a pronounced Bragg peak which is very close to that of stage-2 CsC_{24}.) At ~7.5 kbar CsC_{24} is composed entirely almost of stage-3 domains, and the package thickness starts to decrease again with increasing pressure, as is expected.

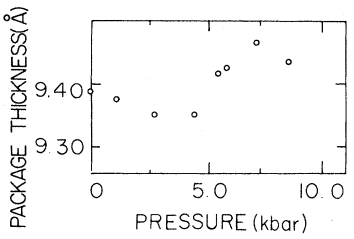

FIG. 5. Package thickness of CsC_{24} calculated from the $2\theta \simeq 13°$ Bragg peak is plotted as a function of hydrostatic pressure (see text).

In order to find the layer structure of Cs atoms, $\vec{q} \perp c$ x-ray experiments were performed using a diffractometer. Because of large background intensities from the Be bases, gasket, and mineral oil, the diffuse x-ray peaks[4] expected from the disordered Cs layers were not observed at ambient pressures. However, at $P > 4$ kbar, both $(h00)$ and $(hk0)$ scans yielded instrumental resolution-limited Bragg peaks at the positions expected from the Cs 2×2 in-plane superlattice. No other Bragg peaks suggesting other superlattice structures were found.

The $(00l)$ x-ray profiles of RbC_{24} taken at several different pressures are shown in Fig. 6. The bottom profile (a) indicates that the starting material was pure stage 2 at ambient pressure. New Bragg peaks of stage-3 domains appear at ~2.5 kbar and develop with increasing pressure, while the stage-2 Bragg peaks diminish. The x-ray profile (e) at 8.1 kbar shows that the sample consists of stage-3 domains with a slight admixture of stage-2 domains.

In both RbC_{24} and CsC_{24} experiments the staging phase transition was completely reversible. It should be emphasized that this indicates that no intercalant atoms were expelled from the sample into the oil pressure-transmitting medium. If the alkali atoms were expelled from the sample, they would surely coalesce in the oil and not reenter the sample. We also report that no apparent irreversible color change was observed in RbC_{24} and CsC_{24} (stage-2 AGIC's are deep blue). Both CsC_{24} and RbC_{24} displayed staging phase transitions similar to the one found in KC_{24}.[14] The staging transition in CsC_{24} occured at higher pressure than in KC_{24} and RbC_{24}. This implies that the repulsive part of the Cs intralayer interaction is strong, possibly due to its large ionic size.

C. Stage 3

Figure 7 shows x-ray diffraction patterns of CsC_{36} obtained at different pressures. The profile (a) taken at 1 kbar shows a typical diffraction pattern of stage-3 CsC_{36}. As pressure increases, some of the small Bragg peaks become indistinguishable from the background, whereas the Bragg peak at $2\theta \simeq 26°$ broadens the splits into two peaks at higher pressures. In order to examine their line shapes the Bragg peaks at $2\theta \simeq 13°$ and 26° are shown expanded in Fig. 8. It is clear now that new peaks evolve very close to the stage-3 $l = 4$ $(2\theta \simeq 13°)$ and $l = 8$ $(2\theta \simeq 26°)$ Bragg peak positions as pressure increases. The stage-3 Bragg peaks exhibit a reduction in their diffracted x-ray intensities and shift to higher 2θ values.

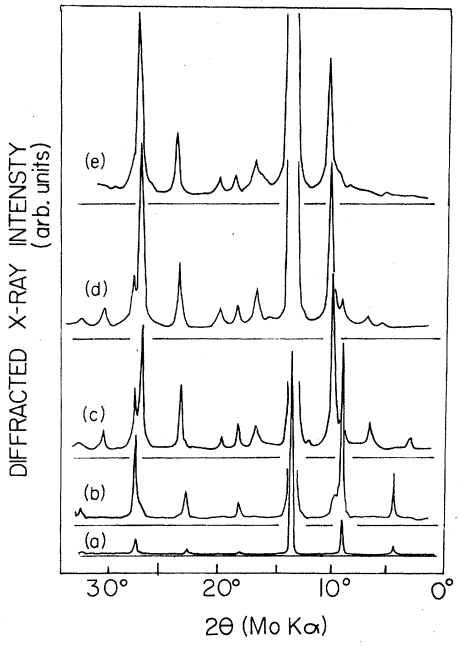

FIG. 6. $(00l)$ x-ray profiles of RbC_{24} taken at (a) 0, (b) 2.5, (c) 4.0, (d) 5.3, and (e) 8.1 kbar.

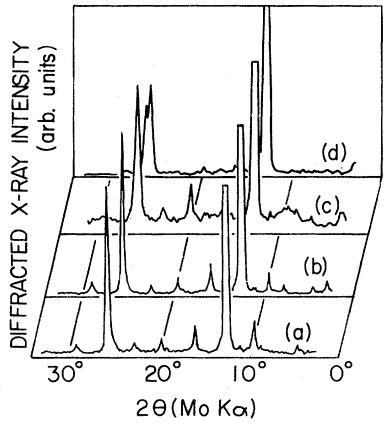

FIG. 7. $(00l)$ x-ray profiles of CsC_{36} taken at (a) 1.6, (b) 6.3, (c) 7.3, and (d) 10.3 kbar.

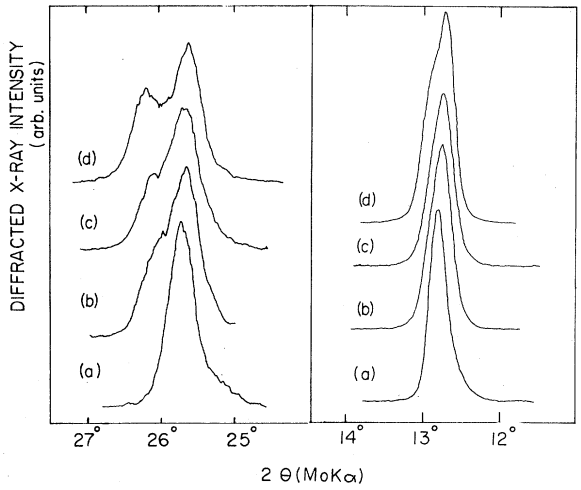

FIG. 8. Expansion of the $2\theta \simeq 13°$ and 26° diffraction peaks in CsC_{36} at (a) 0.0, (b) 5.0, (c) 6.5, and (d) 10.0 kbar.

The lattice contraction of stage-3 domains was found to be ~1.7% at ~10 kbar. We think that these new Bragg peaks arise from stage-4 domains in CsC_{36}, because the package thickness 16.08 ± 0.13 Å obtained at ~10 kbar is very close to the package thickness 16.11 ± 0.05 Å of stage-4 CsC_{48} obtained in this experiment at ambient pressure. Since the dynamics of the ordering process of intercalant layers is unknown, the definition of package thickness of AGIC's during the phase transition is vague. Therefore, we did not attempt to deconvolute the two peaks from the x-ray diffraction profiles in Fig. 8 and obtain compressibilities for each phase.

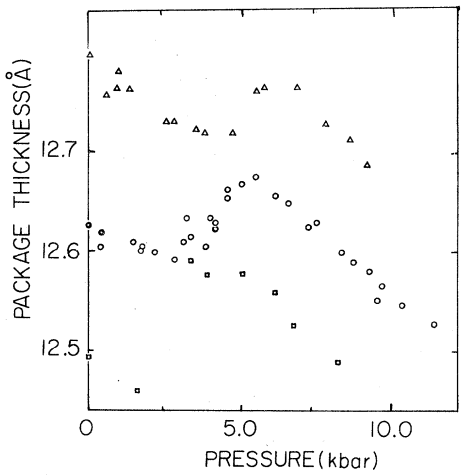

FIG. 9. Calculated package thickness versus pressure for three different CsC_{36} samples, designated as △, ○, and □.

Figure 9 shows a package thickness versus pressure plot of three different CsC_{36} samples. The package thickness was simply calculated from the positions of Bragg peaks at ~13°. Thus, as was the case for CsC_{24}, the staging phase transition is visualized as an increase in the package thickness with pressure. The purpose of this figure is to demonstrate the sample dependence of the package thickness and staging phase transition in CsC_{36}. First, note that the package thickness differs by ~2% from sample to sample, whereas the estimated error of each measurement is less than 0.4%. Secondly, the transition pressure varies from 2.5–5 kbar among these samples. It can be seen from the figure that the sample with a smaller package thickness experienced the staging transition at a lower pressure. Elsewhere,[14] it has been shown that the defects in KC_{24} samples affect the staging phase transition. However, it is not clear why the package thickness varies widely from sample to sample. One possibility is that the stoichiometry of CsC_{36} may not be fixed.

In order to confirm the pressure-induced staging transition, in-plane x-ray experiments were conducted, using both a precession x-ray camera and diffractometer. Figure 10 shows a precession x-ray photograph of CsC_{36} at ~8 kbar at room temperature. The six Bragg spots ($2\theta \simeq 9.55°$)

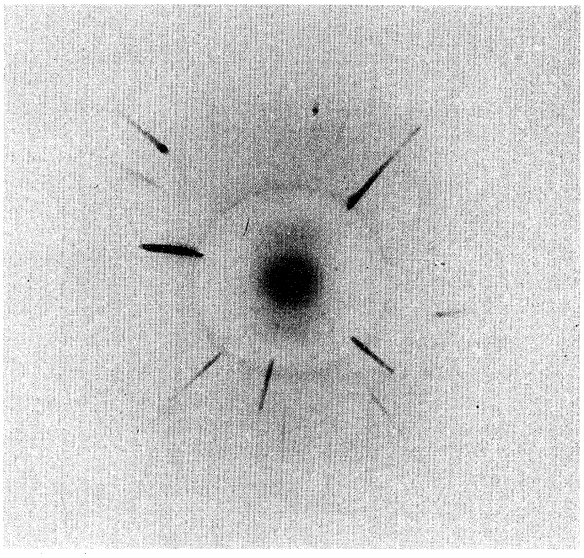

FIG. 10. Precession x-ray photograph of CsC_{36} taken at 8 kbar at room temperature. The c axis of the crystal was approximately parallel to the incident Mo $k\alpha$ incident beam. The six Bragg spots ($2\theta \simeq 9.55°$) are reflections from the ordered Cs superlattice (see text). The intense streaks are x-ray reflections from the diamond anvils and the diffraction ring is from the Be-Cu gasket of the pressure cell.

seen in the picture are identified tentatively as cesium (100) reflections from the Cs 2×2 in-plane superlattice.

The x-ray diffractometer experiments on CsC_{36} yielded the expected graphite in-plane Bragg peaks, but no Cs Bragg peaks at $P<\sim 4.4$ kbar were observed. (The diffuse peaks from the disordered Cs layers were not observed because of the background, as was the case for CsC_{24}.) However, both graphite and Cs in-plane Bragg peaks were found at ~5.5 kbar. At higher pressures, both (h00) and (hk0) in-plane scans confirmed the Cs 2×2 triangular superlattice, but no evidence for other superlattices was found.

Figure 11 shows the (10l) x-ray profiles of CsC_{36}. In contrast to the staging transition in KC_{24},[14] where the c-axis correlations of the superlattice developed with pressure, the profiles in the figure show broad features at high pressures. This indicates no definitive c-axis correlations among these ordered Cs layers. Even after keeping the sample in the diamond cell at ~10 kbar for a month, the (10l) scan did not show any significant development of the c-axis interlayer correlations.

Stage-3 RbC_{36} was also examined by x-ray scattering under high pressure. Figure 12 shows the (00l) x-ray diffraction patterns taken at three different pressures. The x-ray profile (a) shows a pure stage-3 diffraction pattern. Not much change in the profile was observed below ~5 kbar.

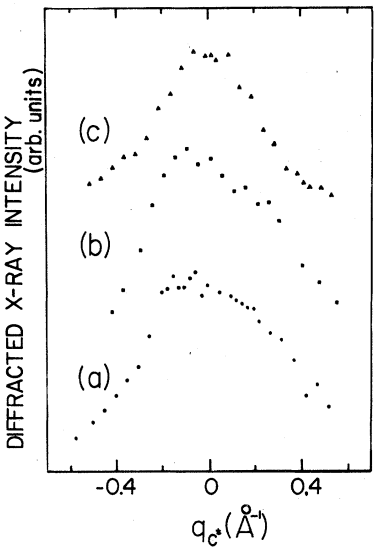

FIG. 11. C_s (10l) x-ray profiles of C_sC_{36} taken at (a) 7, (b) 10, and (c) 10 kbar. The profile (c) was taken from the sample which has been kept at 10 kbar in the diamond cell for one month longer than (b). Note that the geometrical effect of the cell on the diffracted x-ray intensities was not considered.

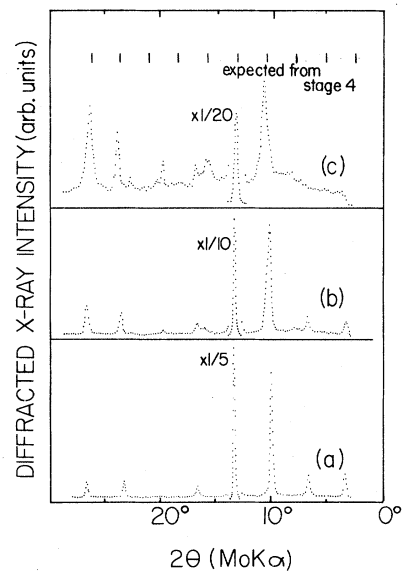

FIG. 12. (00l) x-ray profiles of RbC_{36} taken at (a) 0, (b) 5.3, and (c) 9 kbar. The expected 2θ values from stage-4 domains are also indicated (see text). Note that the abscissa is proportional to $|\vec{q}|$ rather than 2θ.

However, as can be seen from the figure, the Bragg peaks become broader (note that some of the Bragg peaks have an asymetric shape at higher pressures), and some of the Bragg peaks up-shift or down-shift with increasing pressure. For comparison, the expected Bragg positions from stage-4 domains are indicated in the figure. Here, we used the package thickness 15.70 Å obtained in this experiment from stage-4 RbC_{48} at ambient pressure.

Figure 13 shows a plot of the package thickness of RbC_{36} versus pressure. Here again, Bragg's law for the stage-3 $l=3$ and 4 ($2\theta\simeq 10°$ and 13°) peaks was used. Below 4 kbar, the package thicknesses obtained from $l=3$ and 4 did not show a deviation, implying no staging transition. However, at ~5 kbar, there is a sharp increase in the package thickness obtained from the Bragg peak at ~13°, whereas there is a drastic drop in the package thickness from the $2\theta\simeq 10°$ peak. It is interesting to observe a sudden transition in RbC_{36}, since this is quite contrary to the gradual staging transitions described above.

In both CsC_{36} and RbC_{36}, considerable broadening of the (00l) Bragg peaks was observed when pressure was released. [The full width at half maximum (FWHM) of the original peak was less than 0.2° in 2θ, whereas that value for the Bragg peak after releasing pressure was about 0.3°.] In RbC_{36} the stage-3 $l=3$ peak after releasing pressure yielded a different package thickness

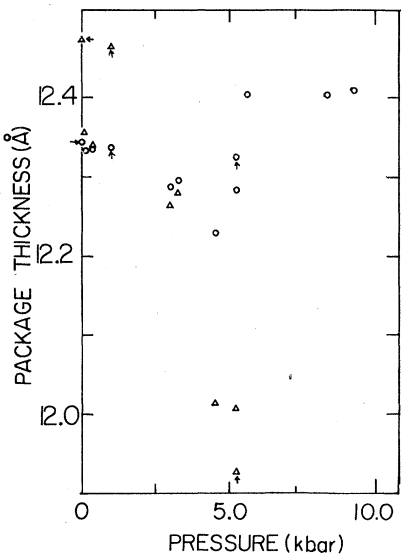

FIG. 13. Package thickness versus pressure plot of RbC_{36}. The values calculated from the $2\theta \simeq 10°$ and 13° diffraction peaks are designated as △ and ○, respectively. The arrows indicate the second-run data points (the sample had experienced the highest pressure).

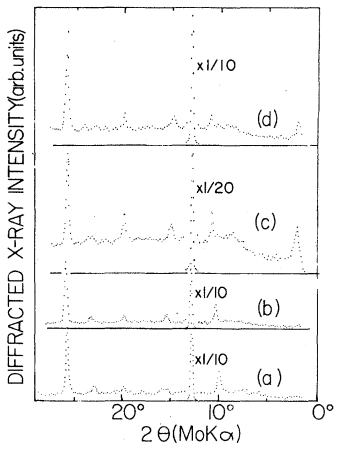

FIG. 14. (00l) x-ray profiles of CsC_{48} taken at (a) 0, (b) 2.1, (c) 7.0, and (d) 10.5 kbar. The profile (a) was taken after releasing pressure. The peak at $2\theta \simeq 20°$ is from the diffuse diffracted ring from the Be-Cu gasket. The abscissa is proportional to $|\vec{q}|$ rather than 2θ.

from the original one, as can be seen in Fig. 13. Since these intercalant atoms can not pass through the graphite hexagons, layer slippages and mismatches play a crucial role in the staging mechanism as was first suggested by Daumas and Hérold.[31] One can imagine that a higher-stage n compound requires more layer slippages and mismatches in order to change the ordered stacking sequence of n graphite layers and an intercalant layer to that of $n+1$ graphite layers an an intercalant layer. We believe that these substantial changes, found after releasing pressure, were caused by the defects produced during the staging transformation. Note that the stage-2 AGIC's dis not show any detectable change after releasing pressure, probably because the mechanical deformation required for staging is minimal in stage-2 compounds compared with higher-stage compounds ($n \geq 3$).

It should be pointed out that if all the Cs layers formed a 2×2 in-plane superlattice in CsC_{36}, then we would expect to observe an even mixture of stage-4 and -5 phases:

$$CsC_{3\times12}(\text{stage 3}) \rightarrow \tfrac{1}{2}CsC_{4\times8}(\text{stage 4}) + \tfrac{1}{2}CsC_{5\times8}(\text{stage 5}). \quad (2)$$

Here the subscripts indicate a stage and a number of carbon atoms per Cs atom in a layer. The same equation should hold for RbC_{36}. However, we did not observe any evidence for stage-5 domains in RbC_{36} and CsC_{36} at these modest pressures.

D. Stage 4

Figure 14 shows the (00l) x-ray profiles of CsC_{48} at different pressures. No drastic change in the profiles can be seen, but some indications of the staging phase transition are apparent. The $2\theta \simeq 10°$ and 23° Bragg peaks (corresponding to the $l = 4$ and 9 Bragg peaks for stage-4 CsC_{48}) shift toward a higher 2θ value, whereas the $2\theta \simeq 16°$ ($l = 6$) peak shifts toward a lower value with increasing pressure. A new peak appears at much lower angle ($2\theta \simeq 2°$) at ~7 kbar. Note that the x-ray profile (a) at 0 kbar obtained after releasing the pressure shows some complicated background. This background may be related to the layer slippages and mismatches during the staging transition, as was discussed above.

To examine the staging transition in CsC_{48} more carefully, the package thickness was calculated from the observed $2\theta \simeq 10°$ and 13° Bragg peaks, using the Bragg equation for stage-4 $l = 4$ and 5, respectively. The results as a function of pressure are shown in Fig. 15. The package thickness obtained from the $2\theta \simeq 13°$ peak stays almost constant with increasing pressure, whereas the one from the $2\theta \simeq 10°$ peak starts deviating at ~3 kbar from the expected value for state-4 CsC_{48}. Above 5 kbar the package thickness from the $2\theta \simeq 10°$ peak also remains almost constant. These results imply that the major staging transformation took place at a pressure range of 3–5 kbar. The package thicknesses obtained from the $l = 4$ and 5 Bragg peaks of above 5 kbar is close to the

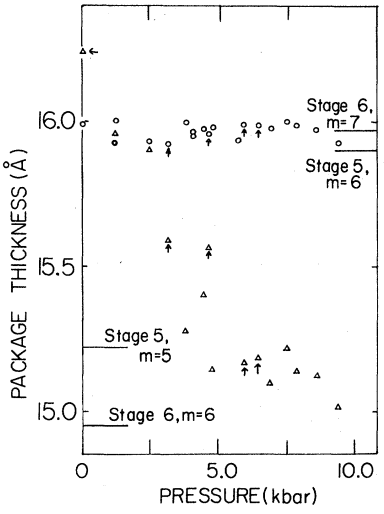

FIG. 15. Package thickness versus pressure plot of CsC_{48}. The values calculated from the $2\theta \simeq 10°$ and 13° diffraction peaks are designated as △ and ○, respectively. The arrows indicate the second-run data points. The expected values from stage-5 and -6 domains are also shown (see text).

"expected" value of stage-5 domains. The expected values in Fig. 15 were obtained by inserting the 2θ value for stage n and mth Bragg peak (n and m values are indicated in Fig. 15) at ambient pressure into the Bragg equations used for those data points. The results at high pressures suggest that the compound consists of stage-5 domains above 5 kbar.

Figure 16 shows the (00l) x-ray profiles of

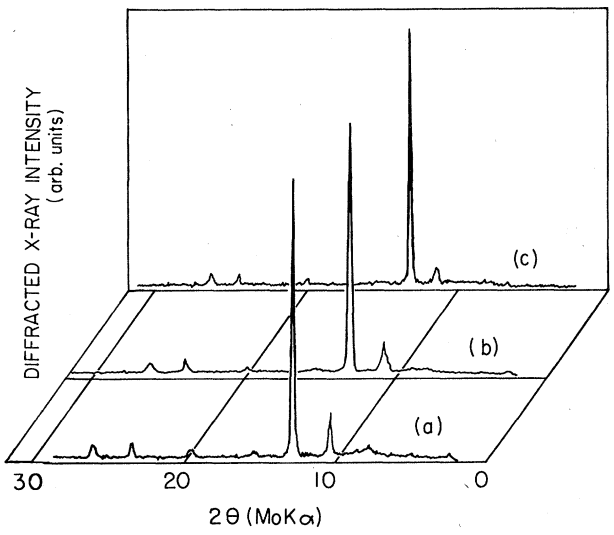

FIG. 16. (00l) x-ray profiles of RbC_{48} taken at (a) 0.7, (b) 4.0, and (c) 9.8 kbar. The diffracted peak at $2\theta \simeq 20°$ is from the Be-Cu gasket.

RbC_{48} taken at different pressures at room temperature. Again, no drastic change can be seen, but, with increasing pressure, some shifts of the Bragg peaks are apparent. The package thicknesses were calculated from the observed $2\theta \simeq 10°$ and 13° Bragg peaks in the same way described above. The plot of package thickness obtained from the $2\theta \simeq 13°$ peak decreases slightly and jumps suddenly at ~7.5 kbar, whereas the value obtained from the $2\theta \simeq 10°$ peak decreases drastically and drops suddenly at ~7.5 kbar. The expected package thicknesses from stage-5 and -6 domains are also shown in Fig. 17. Note that the effect of pressure on lattice compression was not considered when the expected package thicknesses were calculated. If we include the pressure effect, say a 2% contraction of the lattice constant at high pressures, then we find these "observed" package thicknesses in the figure are very close to the expected value of stage 5 at a pressure range of 5–7.5 kbar, and that of stage 6 above 7.5 kbar, as can be seen in the figure. Therefore, we believe that the sample of pure stage-4 RbC_{48} transformed to a mixture of stage-4 and -5 domains and then transformed to a stage-6 phase as pressure was increased. It should be said that if all the Rb atoms form a 2×2 in-plane superlattice, then we will have a pure stage 6,

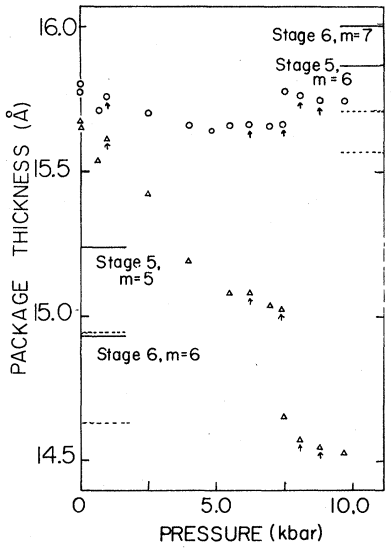

FIG. 17. Package thickness versus pressure plot of RbC_{48}. The values calculated from the $2\theta \simeq 10°$ and 13° diffraction peaks are designated △ and ○, respectively. The arrows indicate second-run data points. The expected values from stage-5 and -6 domains are also shown (see text). The ---- lines indicate the expected values, including the pressure effect (2% lattice contraction which makes the expected values smaller by ~0.3 Å, see text).

as can be seen below:

$$RbC_{4\times12}(\text{stage 4}) \rightarrow RbC_{6\times8}(\text{stage 6}). \quad (3)$$

It is interesting that a sudden transition was also found in RbC_{48} as was the case for RbC_{36}. This is contrary to the gradual staging transitions observed in other compounds.[14] The mechanism by which the high-stage Rb intercalation compounds ($n=3$ and 4) exhibit sudden transitions is not well understood.

Figure 18 also shows in-plane precession photographs of RbC_{48} taken at 0 and 8.8 kbar. No evidence for an ordered structure of Rb layers can be seen at ambient pressure. However, the photograph (b) taken at ~8.8 kbar shows six Bragg peaks at $2\theta \simeq 9.55°$, implying a formation of the 2×2 in-plane superlattice under high pressure. Even in stage-4 RbC_{48}, the same x-ray results for in-plane ordering of intercalant layers were observed.

IV. RAMAN RESULTS AND DISCUSSION

A. Graphite

Figure 19 shows the results for Raman scattering measurements of the pristine graphite intralayer mode, E_{2g} as a function of hydrostatic pressure. The straight line shown in the figure is the best linear fit of the data points. From the slope of this line, the rate of Raman shift with respect to pressure, $\partial\omega_0/\partial P$, was found to be 0.500 (1 ± 0.08) cm^{-1} $kbar^{-1}$. The Raman peak did not show any apparent change in its shape under pressure.

The a-axis component $\gamma_{0\perp}$ of the mode-Grüneisen constants for an anistropic material[32] can be expressed as

$$\gamma_{0\perp} = -\frac{1}{2}\frac{\partial(\ln\omega_0)}{\partial(\ln a)} \simeq -\frac{1}{2}\frac{\Delta(\ln\omega_0)}{\Delta(\ln a)}, \quad (4)$$

where ω_0 is an intralayer phonon mode; a is the a-axis lattice constant. The value $\gamma_{0\perp}$ for the graphite E_{2g} mode was found to be 1.66 ± 0.13, using the elastic constant $C_{11} = (1.056 \pm 0.016) \times 10^{13}$ dyn/cm^2 obtained by Blakslee *et al.*[33] [since $k_a = (1/a_0)(\partial a/\partial P)_{P=0} = 1/C_{11}$].

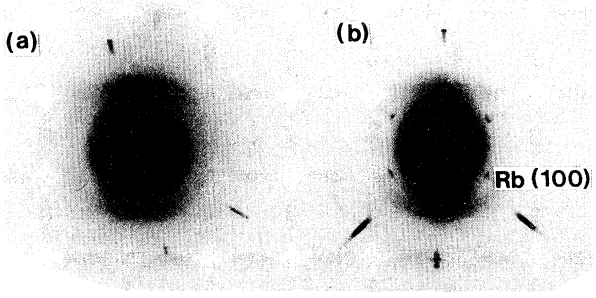

FIG. 18. $\vec{q}\perp c$ precession x-ray photographs of RbC_{48} taken at (a) 0 and (b) 8.8 kbar at room temperature. The reflections from the 2×2 in-plan superlattice are indexed in the photograph (b).

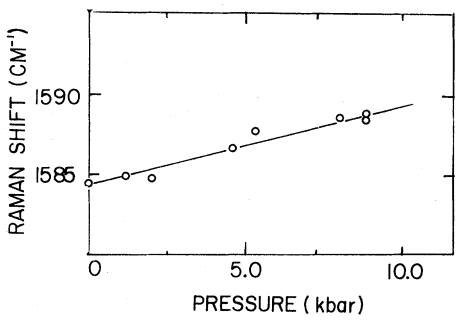

FIG. 19. Raman shift of graphite is plotted as a function of hydrostatic pressure. The straight line indicates the least-squares best fit of the data points.

B. Stage 1

Figure 20 shows the Raman spectra of the 580-cm^{-1} Fano resonance line in stage-1 RbC_8 taken at several different pressures at room temperature. We do not observe any dramatic change in the resonance shape under pressure. This agrees with our x-ray measurements in which no phase transition was found in RbC_8. The resonance shape, however, changes gradually with increasing pressure: The background intensity of the Fano resonance below 580 cm^{-1} diminished, as com-

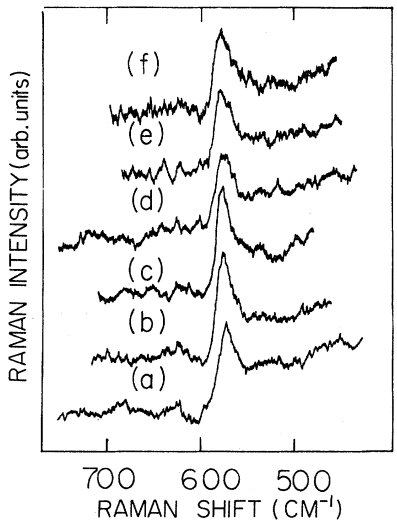

FIG. 20. Raman spectra of the 580-cm^{-1} Fano resonance line in RbC_8, taken at (a) 0, (b) 2.3, (c) 4.3, (d) 6.8, (e) 8.3, and (f) 9.6 kbar.

pared to the background intensity above 580 cm^{-1}. This implies that the continuous density of states, which resonates with the Raman mode, may change substantially with pressure. Also note that the peak position of resonance up-shifts slightly with increasing pressure, as is often the case for Raman peaks of usual materials. We did not analyze the Fano resonance at ~ 1500 cm^{-1} because the pronounced Raman peak at 1333 cm^{-1} from the diamond anvil masked part of the resonance features.

C. Stage 2

The high-pressure Raman spectra of the E_{2g}-like mode in RbC_{24} is shown in Fig. 21. Because there are only type-B graphite layers in stage-2 compounds, the spectrum taken at ambient pressure exhibits one pronounced E_{2g}-like Raman mode at ~1608 cm^{-1}. A new peak evolves gradually at ~1580 cm^{-1} with increasing pressure. This new peak should originate from type-C graphite layers, which have been produced during the staging transformation. Figure 21 gives clear evidence for the pressure-induced staging transition in RbC_{24}. It should be pointed out that the final spectrum (d) in the figure is almost identical to that of stage-3 RbC_{36} at ambient pressure, which will be shown later.

Figure 22 shows the pressure-dependent Raman spectra of E_{2g}-like mode of CsC_{24}. The evolution of the interior Raman mode can be seen, though it is not as clear as in RbC_{24}.

In both RbC_{24} and CsC_{24}, we observe the Raman frequencies increase appreciably with increasing pressure. The plot of Raman frequency versus pressure is shown together with the least-squares best fits in Fig. 23. The numerical results for RbC_{24} and CsC_{24} are tabulated in Table II. Note that the value, $\partial\omega_0/\partial P$ for RbC_{24} is comparable to that of graphite, whereas that value for CsC_{24} is substantially larger than graphite.

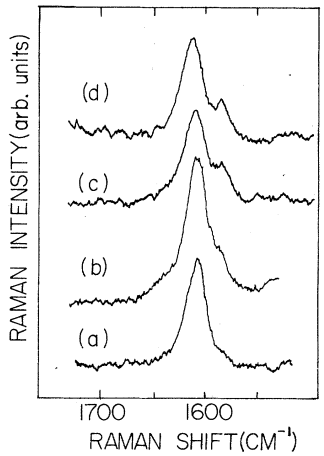

FIG. 21. Raman spectra of RbC_{24} taken at (a) 0.0, (b) 3.8, (c) 5.9, and (d) 8.4 kbar.

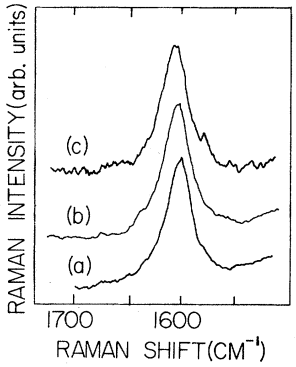

FIG. 22. Raman spectra of CsC_{24} taken at (a) 1, (b) 6.3, and (c) 10.0 kbar.

D. Stages 3 and 4

Figure 24 shows the Raman spectra of RbC_{36} taken at several different pressures. As we predicted, the relative ratio of integrated intensity of the interior mode (~1582 cm^{-1}) to that of the bounding mode (~ 1609 cm^{-1}) increases with pressure. As a result of the change in the c-axis stacking sequence during the staging transtion, the number of interior graphite layers (type C) increases, whereas that of bounding layers (type B) decreases. Therefore, the Raman intensities which are proportional to the number of particular layers vary accordingly in the phase transition.

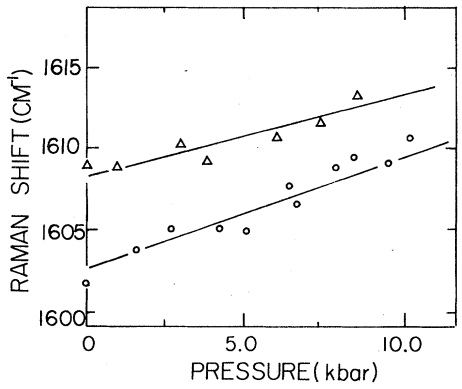

FIG. 23. Raman shifts of the bounding modes in CsC_{24} and RbC_{24} (designated as △ and ○, respectively) are plotted as a function of hydrostatic pressure. The least-squares best fits for each set of data points are also shown.

TABLE II. The zero-pressure Raman frequency (ω_0) and the rates of Raman frequency shifts with respect to pressure, ($\partial\omega_0/\partial P$) of graphite, CsC_{24}, and RbC_{12n} ($n=2,3,4$).

	Mode	ω_0 (cm^{-1})	$\partial\omega_0/\partial P$ ($cm^{-1}\,kbar^{-1}$)
Graphite	E_{2g}	1584	0.50 ± 0.04
CsC_{24}	bounding	1603	0.70 ± 0.12
RbC_{24}	bounding	1608	0.51 ± 0.09
RbC_{36}	interior	1582	0.78 ± 0.08
	bounding	1609	0.44 ± 0.05
RbC_{48}	interior	1584	0.32 ± 0.12
	bounding	1609	0.54 ± 0.08

Figure 25 shows the pressure-dependent Raman spectra of RbC_{48}. The pressure-induced staging transition is revealed by the dramatic change in the relative intensities of the interior and bounding modes. The Raman spectrum (f) in the figure, which was taken after releasing pressure, shows similar features to the spectrum (a) taken at 2.2 kbar. This proves that the staging transition is reversible. In other Raman experiments mentioned above, the reversibility of the transition was also confirmed.

The plots of Raman frequency versus pressure for RbC_{36} and RbC_{48} are shown in Fig. 26. For each mode, the least-squares best fits were calculated and shown in the figure. The numerical values obtained are also tabulated in Table III. Since no data for the a-axis compression in AGIC's are available, the mode-Grüneisen constants for each mode were not obtained. The experimental values $\partial\omega_0/\partial P$ for both RbC_{36} and RbC_{48} exterior modes were found to be similar to that of pristine graphite. However, interestingly, the values $\partial\omega_0/\partial P$ for the interior modes or RbC_{36} (0.78 cm^{-1} $kbar^{-1}$) and RbC_{48} (0.32 $cm^{-1}\,kbar^{-1}$) are much different from that of graphite (0.50 $cm^{-1}\,kbar^{-1}$). These differences may be associated with charge delocalization.[34] The experimental results suggest that the c-axis charge distribution around the interior graphite layers may differ substantially from one stage to another.

Since the high-stage AGIC's ($n \geq 2$) are ordered at high pressures, the zone-folding theory[19,20] which predicts some new off-zone-center Raman peaks might be applied. In the theory, because

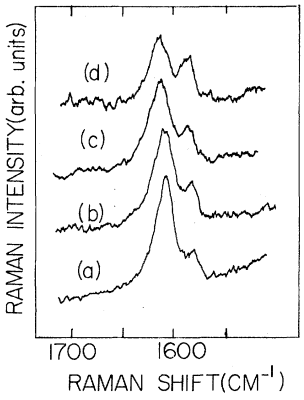

FIG. 24. Raman spectra of RbC_{36} taken at (a) 0, (b) 3.0, (c) 4.8, and (d) 7.6 kbar.

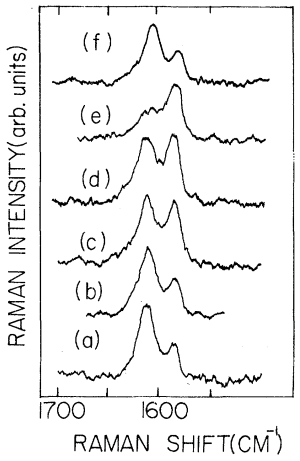

FIG. 25. Raman spectra at RbC_{48} taken at (a) 2.2, (b) 3.3, (c) 5.3, (d) 8.8, (e) 9.8, and (f) 0 kbar. The spectra were taken consecutively.

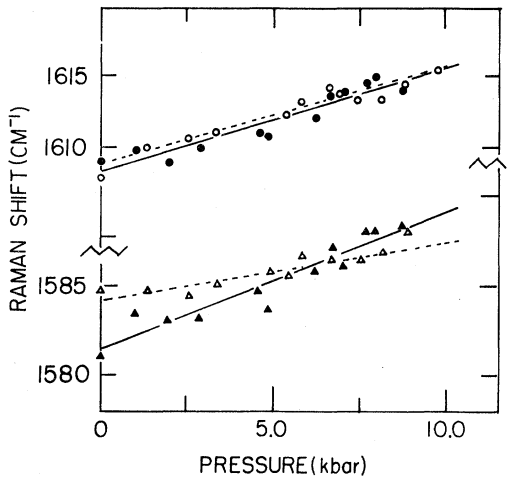

FIG. 26. Raman shifts of RbC_{36} (▲ and ●) and RbC_{48} (△ and ○) are plotted as a function of hydrostatic pressure. The —— and ---- lines correspond to the least-squares best fits of the RbC_{36} and RbC_{48} data points, respectively.

of the superlattice structure in the ordered GIC's, the phonon dispersion curves of graphite can be folded and produce new zone-center phonon modes. Some of these modes are Raman active, e.g. those at the M point of the original zone. Dresselhaus *et al.*[19,20] attributed the Fano resonance features in stage-1 AGIC's to the resonance of the zone-folded phonons with a continuum. Therefore, we attempted to look for new Raman peaks in those compounds at high pressures. However, no evidence for new Raman features was found.

V. CONCLUDING REMARKS

Remarkable pressure effects on staging of high-stage AGIC's MC_{12n} (M = Rb and Cs and $n = 2, 3, 4$) have been revealed, using both x-ray and Raman techniques. The pressure-induced staging phase transition was found to be universal among the AGIC's ($n \geq 2$) with characteristics of reversibility, hysteresis, and sample dependence. The formation of 2×2 in-plane superlattices and rearrangement of c-axis stacking sequences suggest qualitative agreement for the high-pressure effects implied from the dipole theory for staging.[13] However, it is difficult to quantitatively analyze the inter and intralayer interactions in AGIC's under pressure because of the simultaneous occurence of intercalant intra- and interlayer ordering, and of the nature of the phase transition (large hysteresis and sample dependence).

It is interesting that the well defined stages, evidenced by the narrow ($00l$) Bragg peaks, persist during the staging transitions in which many slippages and mismatches of layers are anticipated. There must be a very effective intercalant interlayer interaction in AGIC's. However, the c-axis correlation of the 2×2 in-plane superlattices of high-stage AGIC's ($n \geq 3$) seems poor [the ($10l$) scans of CsC_{36} showed broad features in the diffraction pattern]. This may imply severe stacking faults and defects. It would be interesting to study the growth of intralayer ordering of intercalant atoms with increasing pressure.

Finally, we point out that high-pressure experiments with changing temperature will potentially explore more fascinating fundamentals of physics in GIC's. In low-temperature experiments,[2-6] no staging transitions were found when ordering of intercalant layers occurred with decreasing temperature. This means we can possibly control the staging and ordering by adjusting both temperature and pressure. Another speculative aspect concerns a melting phase transition. Bak[35] indicated the possibility of 3D continuous melting in EuC_6. It would, therefore, be interesting to see how high-pressure ordered phases of AGIC's ($n \geq 2$) melt with temperature.

ACKNOWLEDGMENTS

The author wishes especially to thank Professor S. A. Solin for his advice and support during the completion of this project. Useful discussions with Roy Clarke, D. M. Hwang, N. Caswell, and S. R. Nagel are gratefully acknowledged. Thanks are also due to J. Pluth for technical assistance and J. G. Hooley for providing the single crystals used in this experiment. M. D. Beals of Lazare Kaplan & Sons, Inc. has been very helpful in providing diamond anvils for this Raman experiment. This work was supported by the US AROD under Grant No. DAAG 29-80-K-0003 and by the NSF under Grant No. DMR 80-10486. Support of the University of Chicago Materials Research Laboratory is also acknowledged.

---

*Submitted in partial fulfillment of the requirements for the Ph.D. degree at the University of Chicago. Present address: The Materials Research Laboratory and Coordinated Science Laboratory, University of Illinois at Urbana-Champaign, Urbana, Illinois 61801.

[1]See Physica B 99 (1980), references therein.
[2]Roy Clarke, N. Caswell, and S. A. Solin, Phys. Rev. Lett. 42, 61 (1979).
[3]J. B. Hasting, W. D. Ellenson, and J. E. Fischer, Phys. Rev. Lett. 42, 1552 (1979).
[4]Roy Clarke, N. Caswell, S. A. Solin, and P. M. Horn, Phys. Rev. Lett. 43, 2018 (1979).
[5]H. Zabel, S. C. Moss, N. Caswell, and S. A. Solin, Phys. Rev. Lett. 43, 2022 (1979).
[6]S. A. Solin, Adv. in Chem. Phys., in press.
[7]W. Metz and D. Holwein, Carbon 13, 87 (1975).
[8]W. Rüdorff and E. Schulze, Z. Anorg. Allg. Chem. 277, 156 (1954).
[9]S. A. Safran, Phys. Rev. Lett. 44, 937 (1980).
[10]N. Caswell, Phys. Rev. B 22, 6308 (1980).
[11]H. Zabel, Y. M. Jan, and S. C. Moss, Physica B 99, 453 (1980).
[12]N. Caswell, S. A. Solin, T. M. Hayes, and S. J. Hunter, Physica B 99, 463 (1980).
[13]S. A. Safran and D. R. Hamann, Phys. Rev. Lett. 43, 1410 (1979).
[14]Roy Clarke, N. Wada, and S. A. Solin, Phys. Rev. Lett. 44, 1616 (1980).
[15]S. A. Solin and N. Caswell, J. Raman Spectrosc., in press.
[16]R. J. Nemanich, S. A. Solin, and D. Guérard, Phys. Rev. B 15, 6014 (1977).
[17]P. C. Eklund and K. R. Subbaswamy, Phys. Rev. B 20, 5157 (1979).

[18]N. Caswell and S. A. Solin, Phys. Rev. B 20, 2551 (1979).
[19]M. S. Dresselhaus and G. Dresselhaus, in *Physics and Chemistry of Materials with Layered Structures*, edited by F. Levy (Reidel, Dordecht, Holland, 1979), Vol. 6.
[20]M. S. Dresselhaus, G. Dresselhaus, P. C. Eklund, and D. D. L. Chung, Mater. Sci. Eng. 31, 141 (1977).
[21]D. E. Nixon and G. S. Parry, J. Phys. C 2, 1732 (1969).
[22]H. Miyazaki, T. Hatano, G. Kusunoki, T. Watanabe, and C. Horie, Physica B, in press.
[23]A. Hérold, Bull. Soc. Chim. Fr. 187, 999 (1955).
[24]L. Merrill and W. A. Bassett, Rev. Sci. Instrum. 45, 290 (1974).
[25]Bernard A. Weinstein and G. J. Piermarini, Phys. Rev. B 12, 1172 (1975).
[26]R. Loudon, Adv. Phys. 13, 423 (1964).
[27]N. Wada, Roy Clarke, and S. A. Solin, Solid State Commun. 35, 675 (1980).
[28]W. D. Ellenson, D. Semmingser, D. Gruérard, D. G. Onn, and J. E. Fischer, Mat. Sci. Eng. 31, 137 (1977).
[29]C. D. Fuerst, W. D. Johnson and J. E. Fischer, in Proceedings of the Fourteenth Biennial Conference on Carbon, Pennsylvania, 1979, unpublished.
[30]N. Kambe, H. Mazurek, M. S. Dresselhaus, and G. Dresselhaus, Physica B, in press.
[31]N. Daumas and A. Hérold, C. R. Acad. Sci. 268, 373 (1968).
[32]T. H. K. Barron and R. W. Munn, Philos. Mag. 15, 85 (1917).
[33]O. L. Blakslee, D. G. Proctor, E. J. Seldin, G. B. Spence, and T. Weng, J. Appl. Phys. 41, 3373 (1970).
[34]J. E. Fischer and T. E. Thompson, Phys. Today 31 (7), 36 (1978).
[35]Per. Bak, Phys. Rev. Lett. 44, 889 (1980).

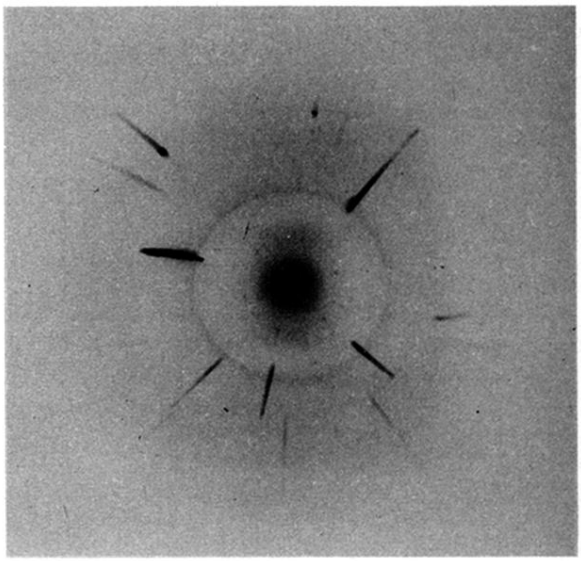

FIG. 10. Precession x-ray photograph of CsC_{36} taken at 8 kbar at room temperature. The c axis of the crystal was approximately parallel to the incident Mo $k\alpha$ incident beam. The six Bragg spots ($2\theta \simeq 9.55°$) are reflections from the ordered Cs superlattice (see text). The intense streaks are x-ray reflections from the diamond anvils and the diffraction ring is from the Be-Cu gasket of the pressure cell.

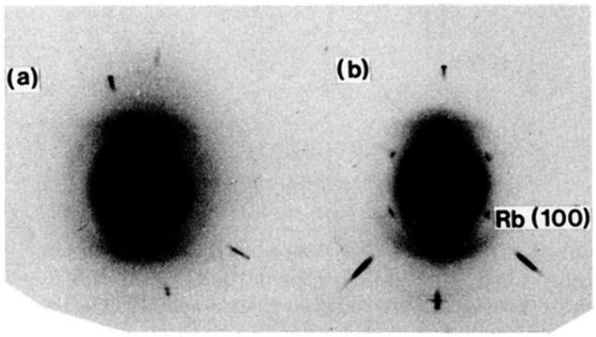

FIG. 18. $\vec{q} \perp c$ precession x-ray photographs of RbC_{48} taken at (a) 0 and (b) 8.8 kbar at room temperature. The reflections from the 2×2 in-plan superlattice are indexed in the photograph (b).